



Cite this: *RSC Adv.*, 2025, **15**, 36145

## Novel hierarchical $Mn_xO_y$ -functionalized graphene for enhanced visible-light photodegradation performance

Pham Huong Quynh,<sup>a</sup> Ta Thi Huong,<sup>a</sup> Tran Y Doan Trang,<sup>a</sup> Pham Thi Mai Huong,<sup>a</sup> Nguyen Thi Thu Phuong,<sup>\*,a</sup> Pham Nguyet Anh,<sup>b</sup> Nguyen Thanh Trung,<sup>c,d</sup> Vu Thi Thuy,<sup>ef</sup> Dang Van Thanh<sup>fg</sup> and Nguyen Long Tuyen<sup>\*,h</sup>

Novel hierarchical  $Mn_xO_y$ -functionalized graphene photocatalysts were successfully synthesized by simultaneous precipitation combined with electrochemical plasma methods. Comprehensive characterization, such as XRD, Raman, FT-IR, XPS, SEM, and TEM results, showed the formation of hierarchically structured  $Mn_xO_y$ -graphene nanocomposites (GMP) via a change in the pH of the initial solution. The visible-light photodegradation performance of the as-prepared GMP was significantly enhanced compared to that of their counterparts owing to the synergistic effects of graphene and  $Mn_xO_y$ . Specifically, the GMP10 sample displayed the highest efficiency for methylene blue decomposition, reaching 84.5% after 150 minutes of illumination. The stability of the material was confirmed through four consecutive degradation cycles, during which the efficiency of methylene blue degradation decreased by 6.9% (from 84.5% to 77.6%).

Received 6th May 2025  
 Accepted 17th September 2025

DOI: 10.1039/d5ra03186a  
[rsc.li/rsc-advances](http://rsc.li/rsc-advances)

## 1 Introduction

Manganese oxides ( $Mn_xO_y$ ), including  $MnO$ ,  $Mn_3O_4$ ,  $Mn_2O_3$ ,  $MnO_2$ , and similar components, have been widely studied for their practical applications in adsorption,<sup>1</sup> supercapacitors,<sup>2,3</sup> photocatalysis<sup>4,5</sup> due to the advantages of low cost, easy availability, low toxicity, large surface area, and high specific capacitance. However, their poor electronic conductivity and structural instability under various synthesis conditions hinder their applications.<sup>6</sup> To overcome these obstacles, carbon materials, especially graphene, have been functionalized with  $Mn_xO_y$  to take advantage of their synergistic effects in boosting electrocatalytic activity, catalyzing the decomposition of organic substances, and facilitating the charge storage process in supercapacitors.<sup>7,8</sup> As a result, many methods have been

developed to prepare hybrid materials, such as the sol-gel method,<sup>9</sup> solvothermal method,<sup>10</sup> hydrothermal method<sup>11</sup> and microwave irradiation.<sup>12</sup> These different approaches influence particle size distribution, particle morphology, nanoparticle dispersion, and the bonding between nanoparticles and the graphene layer, thus affecting the overall characteristics of the material. For example, Yingxi *et al.* used three methods to fabricate graphene-supported metal oxide nanomaterials: direct impregnation, homogeneous oxidative precipitation with hydrogen peroxide, and ammonia-catalyzed hydrolysis.<sup>13</sup> The authors demonstrated that the ammonia-catalyzed hydrolysis method produced large and uneven particle sizes, whereas the oxidative precipitation approach resulted in uniform particle sizes and the best dispersion. The materials obtained by these three methods exhibited different catalytic activities depending on their particle size. The research also indicated that parameters such as temperature, reaction time, and pH significantly influenced the structure and properties of the final material. Recently, Atif *et al.* reported the green synthesis of  $MoO_3$  and  $MnO$  nanoparticles on graphene oxide, resulting in efficient photocatalysts. They found that GO/MnO demonstrated the highest removal efficiency of 98% for methylene blue (MB), significantly greater than that of pure  $MnO$  (60%).<sup>14</sup> Jarvin *et al.* successfully prepared an  $Mn_3O_4$ -rGO nanocomposite by the solvothermal method, and the as-synthesized material achieved a good photocatalytic dye degradation efficiency of 60% within 120 min.<sup>15</sup> Moreover,  $Mn_2O_3$  anchored on graphitic carbon nitride was reported by Lalitha and colleagues.<sup>16</sup> GCN-decorated

<sup>a</sup>Hanoi University of Industry, 298 Cau Dien Street, Bac Tu Liem District, Hanoi 100000, Vietnam. E-mail: phuongntt@hau.edu.vn

<sup>b</sup>Thuyloi University, 175 Tay Son Street, Dong Da District, Hanoi 100000, Vietnam

<sup>c</sup>Institute of Physics, Vietnam Academy of Science and Technology, Vietnam Academy of Science and Technology, 18 Hoang Quoc Viet, Hanoi 10072, Vietnam

<sup>d</sup>Research and Development Center for Advanced Technology, Ha Noi, Vietnam

<sup>e</sup>Institute of Science and Technology, TNU-University of Sciences, Tan Thinh Ward, Thai Nguyen 24000, Vietnam

<sup>f</sup>Faculty of Basic Sciences, TNU-University of Medicine and Pharmacy, 284 Luong Ngoc Quyen St., Thai Nguyen, Vietnam

<sup>g</sup>VNU Key Laboratory of Green Environment, Technology and Waste Utilization (GreenLab), University of Science, Vietnam National University, Hanoi, Vietnam

<sup>h</sup>Hung Vuong University, Nong Trang, Viet Tri City, Phu Tho 35000, Vietnam. E-mail: [nguyenlongtuyen@hvu.edu.vn](mailto:nguyenlongtuyen@hvu.edu.vn)



$\text{Mn}_2\text{O}_3$  exhibited excellent photocatalytic performance for MB degradation.

Electrochemical discharge, a hybrid of electric discharge and electrolysis, is widely used for nanomaterial synthesis. Co-precipitation, a simple and cost-effective technique, enables the preparation of high-purity compounds with tailored structures due to its simplicity in device design, its low cost, and minimal equipment requirements for nanomaterial fabrication. Since plasma-liquid interactions involve both plasma and liquid, the properties of the final product can be tuned by adjusting the plasma parameters or the composition of the electrolyte medium, or by co-precipitation in the reaction solution. To the best of our knowledge, the use of electrochemical discharge and co-precipitation to effectively tune the Mn valence on graphene to provide an efficient photocatalyst has not yet been investigated.

Therefore, in this study, we hypothesize that Mn with multiple valence states can be effectively tuned during the co-precipitation reaction of Mn-containing salt precursors with the plasma-reacting electrolyte for synthesizing  $Mn_xO_y$ /graphene by pH adjustments. Furthermore, these  $Mn_xO_y$ /graphene compounds exhibited higher catalytic efficiency than single-phase  $Mn_xO_y$  when tested using methylene blue (MB) dye as a simulated wastewater model.

## 2 Experiments

Manganese oxide was prepared using the conventional co-precipitation method. Solution (1) was a mixture of 200 mL of NaOH solution (10%) and 50 mL of  $(\text{NH}_4)_2\text{SO}_4$  solution (5%), with the pH adjusted to 12. Solution (2) was  $\text{MnCl}_2$  solution (2 M) dropped into mixture (1) at a rate of  $\sim 1$  drop/s. Ultrasonic vibration was then applied continuously during the dropwise

addition and for an additional 30 minutes. The resulting material was denoted as  $Mn_xO_y$ .

### 3 Results and discussion

Fig. 1(a) shows the XRD patterns of the  $Mn_xO_y$  and graphene/ $Mn_xO_y$  composite samples. The  $Mn_xO_y$  sample was indexed to the tetragonal  $Mn_3O_4$  structure (JCPDS No. 151-4120), and its diffraction peaks appeared in the composite samples, confirming the presence of  $Mn_3O_4$ . However, the composite samples also exhibited additional peaks indicating the presence of monoclinic  $MnOOH$  (JCPDS No. 900-9774) and  $MnO_2$  (JCPDS No. 901-6546). The sharp diffraction peaks indicated that the product was well-crystallized. From GMP8 to GMP12, the intensity ratio of the  $26.1^\circ$  peak ( $MnOOH$  phase) to the  $36.1^\circ$  peak ((211) facet of  $Mn_3O_4$ ) gradually increases, implying decreased  $Mn_3O_4$  crystallinity and increased  $MnOOH$  formation. Furthermore, the graphene peak at  $26.01^\circ$  overlaps with the  $26.1^\circ$  peak ((001) facet of  $MnOOH$  or (110) facet of  $MnO_2$ ), broadening the peak and confirming the presence of graphene. The XRD results show that the composite samples prepared by the plasma-assisted electrochemical exfoliation method contained additional components, such as  $MnOOH$  and  $MnO_2$ , in addition to the  $Mn_3O_4$  component. In contrast, the  $Mn_xO_y$  samples prepared by the chemical precipitation method consisted solely of the  $Mn_3O_4$  phase. The appearance of  $MnOOH$  and  $MnO_2$  in the composite samples was believed to result from the plasma discharge process and the change in the solution pH.

The FT-IR results in Fig. 2(b) were used to investigate the bonding structures of the samples. For the graphene sample, the  $1575\text{ cm}^{-1}$  absorption peak corresponds to the aromatic C=C stretching vibration, which shifts to higher wavenumbers

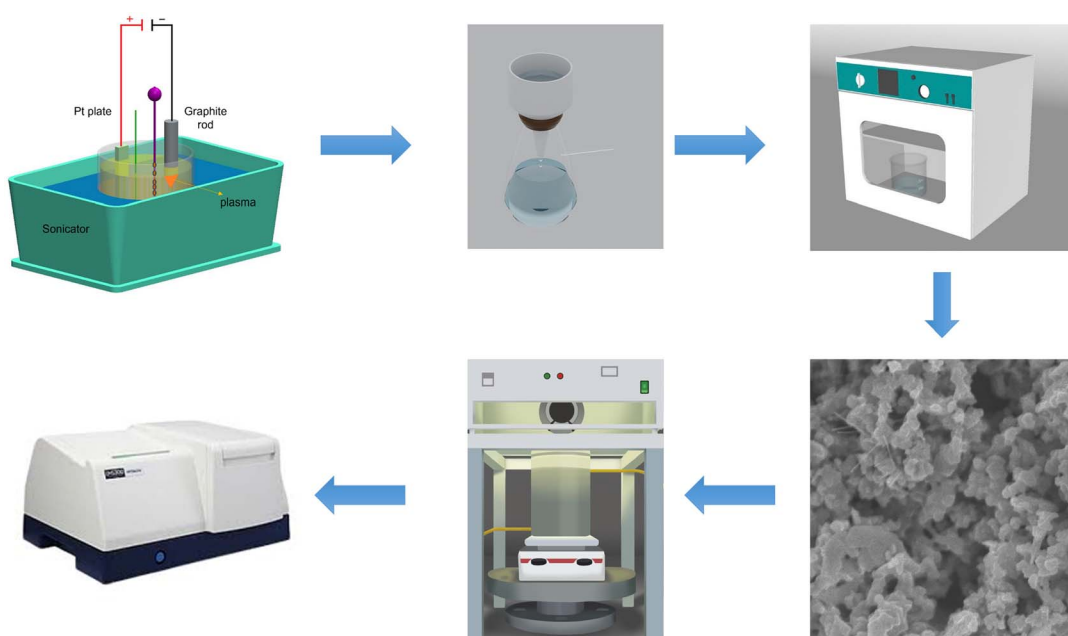


Fig. 1 Schematic of  $\text{Mn}_x\text{O}_y$ /graphene and photocatalytic degradation of MB

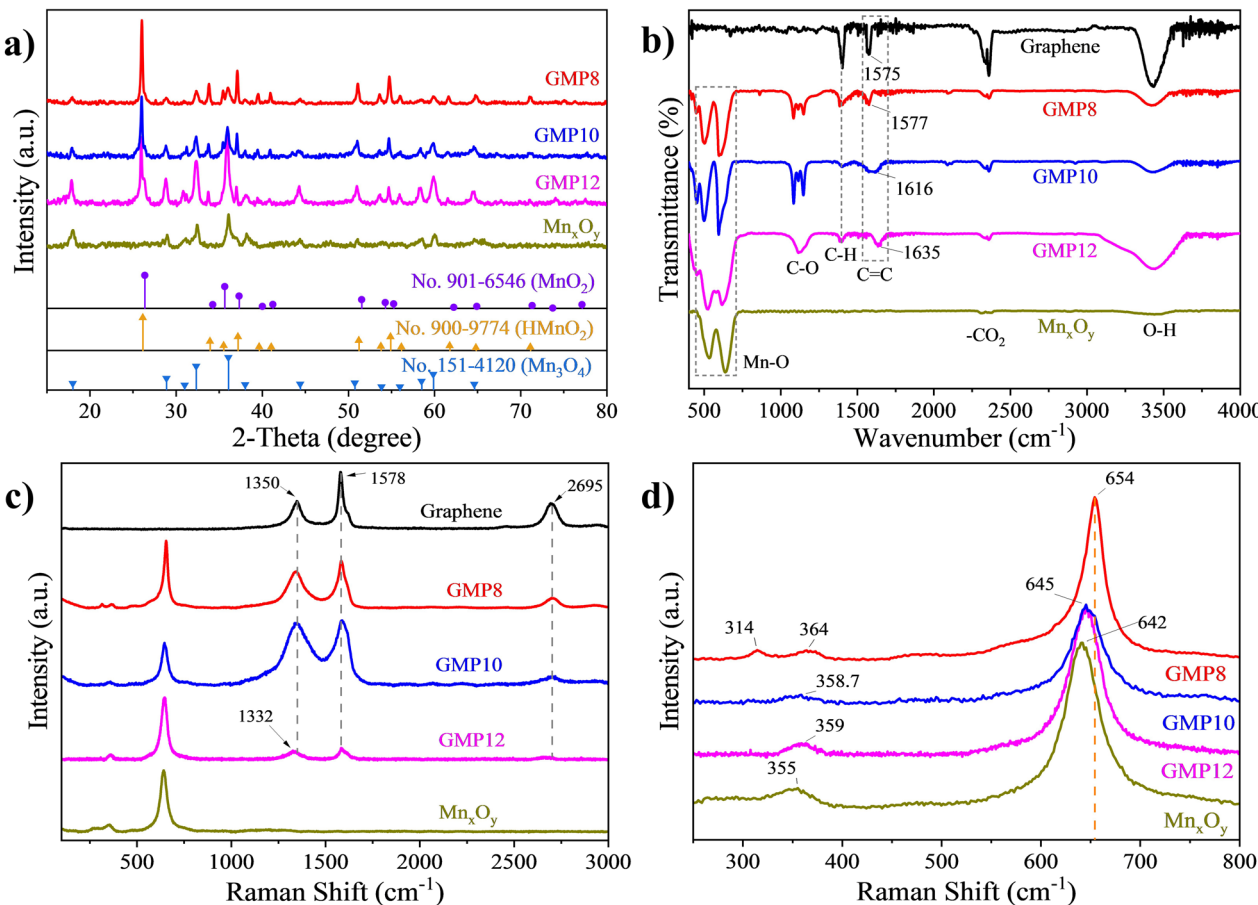


Fig. 2 (a) XRD patterns; (b) FT-IR spectra and (c) Raman spectra of graphene,  $Mn_xO_y$ , and GMP8–GMP10 composite materials; and (d) extended Raman spectra from part (c).

and broadens in the case of the composites. Additionally, the peaks at  $497\text{--}533\text{ cm}^{-1}$  and  $593\text{--}638\text{ cm}^{-1}$  in the spectra of the  $Mn_xO_y$  and composite samples were attributed to the Mn–O bond vibrations and O–Mn–O stretching, respectively,<sup>17,18</sup> confirming the coexistence of graphene and manganese oxide. Fig. 2(c and d) shows the Raman spectra of graphene,  $Mn_xO_y$ , and their hybrid samples. Both graphene and the composites exhibit D bands ( $1348\text{ cm}^{-1}$ ) and G bands ( $1578\text{ cm}^{-1}$ ), corresponding to the breathing mode of the carbon rings and the stretching mode of the  $sp^2$  carbon atoms. However, the  $I_D/I_G$  intensity ratios for the GMP8 (0.78), GMP10 (0.85), and GMP12 (0.83) composite samples were higher than that of the graphene sample (0.52), indicating that  $Mn_xO_y$  could be incorporated into the graphene structure, thereby increasing the degree of defects. Typical  $Mn_xO_y$  bands were also observed; for example, GMP8 showed a peak at  $642\text{ cm}^{-1}$ , attributed to Mn–O stretching in the octahedral  $MnO_6$  structure of  $MnO_2$ , while GMP12 exhibited a  $654\text{ cm}^{-1}$  band indicative of Mn–O vibrations in the spinel  $Mn_3O_4$  structure. The slight shift in this peak for the other composites possibly resulted from the mixing of the different components.

The XPS spectra were used to determine the oxidation state and composition of the  $Mn_xO_y$  material and GMP8–GMP12 composites. As presented in Fig. 3(a), the  $Mn_xO_y$  sample showed

two O 1s peaks at  $530.2\text{ eV}$  and  $531.7\text{ eV}$ , corresponding to the lattice oxygen of  $Mn_3O_4$  and surface-adsorbed oxygen, respectively, confirming its pure  $Mn_3O_4$  phase, as observed using XRD. In contrast, the GMP8–GMP12 composites exhibited four O 1s peaks at  $529.6$ ,  $530.2$ ,  $531.3$ – $531.5$ , and  $532.9$ – $533.5\text{ eV}$ , which correspond to O–Mn<sup>4+</sup> bonds,  $Mn_3O_4$  lattice oxygen, surface hydroxyl groups ( $Mn$ –OH/C–OH), and adsorbed water, respectively.<sup>19,20</sup> These findings indicate that the composites contained both Mn<sup>4+</sup> and Mn<sup>3+</sup> ( $Mn_3O_4$ ) components. Fig. 3(b) shows the Mn 2p spectra of the  $Mn_xO_y$  sample, featuring Mn 2p<sub>3/2</sub> and Mn 2p<sub>1/2</sub> peaks at  $641.5\text{ eV}$  and  $653.3\text{ eV}$ , respectively, whereas in the composites, these peaks were shifted to  $642.2$ – $642.3\text{ eV}$  and  $653.9$ – $654\text{ eV}$  due to the formation of Mn<sup>4+</sup> ( $MnO_2$ ) bonds. The energy separation of  $11.8\text{ eV}$  for  $Mn_xO_y$  and  $11.7\text{ eV}$  for the composites is consistent with previous  $Mn_3O_4$  data.<sup>21,22</sup> Fig. 3(c) presents the high-resolution C 1s spectra of the GMP8–GMP12 composites deconvoluted into three peaks at  $284.5\text{ eV}$  (C=C/C–C),  $285.7$ – $286.2\text{ eV}$  (epoxy C–O), and  $287.9$ – $288.5\text{ eV}$  (carbonyl C=O).<sup>23</sup> The low intensity of the C–O and C=O peaks indicates that graphene is in a low oxidation state.

The SEM and TEM images in Fig. 4(a and c) clearly show agglomeration of the  $Mn_xO_y$  nanoparticles. In contrast, GMP10 contains a large number of  $Mn_xO_y$  nanoparticles (20–80 nm) anchored on the graphene sheets (Fig. 4(b)). The TEM images of

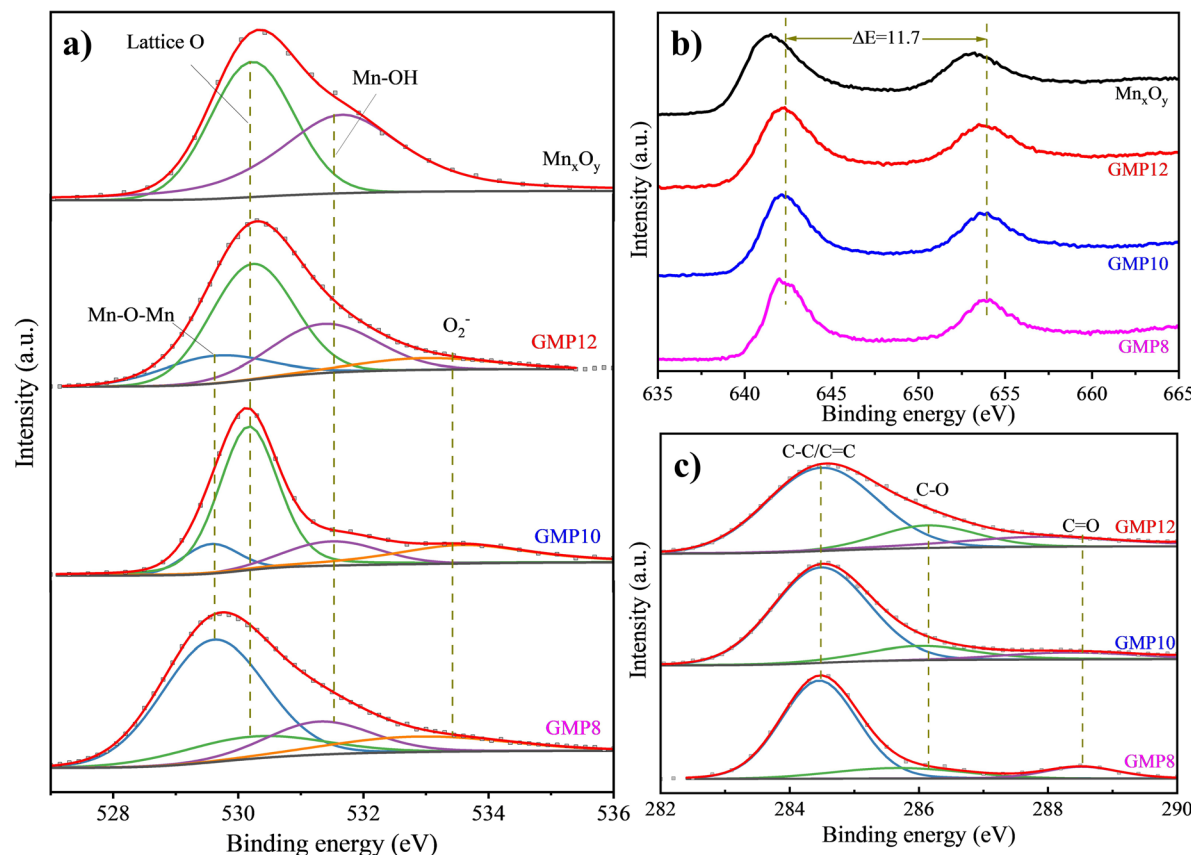


Fig. 3 XPS spectra of  $\text{Mn}_x\text{O}_y$  and GMP8–GMP12 nanocomposite samples: (a) O 1s; (b) Mn 2p and (c) C 1s.

GMP10 also verify the numerous folds at the edges of the graphene sheets (Fig. 4(d)), revealing a generally homogeneous shape with some pores. The combination of the graphene sheets with the  $\text{Mn}_x\text{O}_y$  nanoparticles reduced material

agglomeration while increasing the porosity of the composite, thereby enhancing its photocatalytic activity. The interplanar spacings of 0.264 nm and 0.288 nm were well observed, corresponding to the (202) plane of  $\text{HMnO}_2$  and the (200) plane of

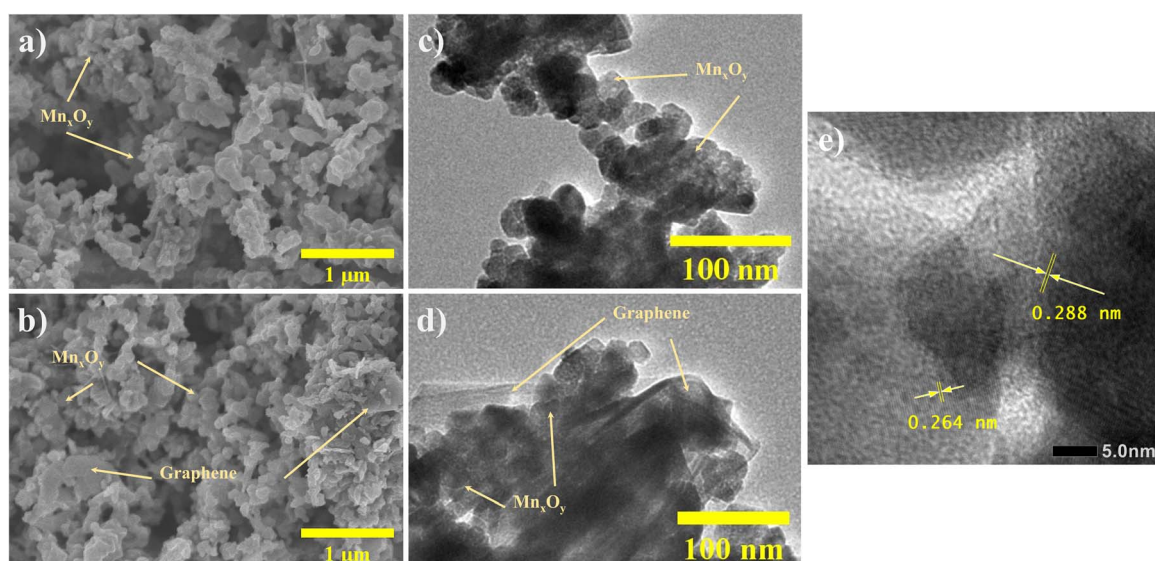


Fig. 4 SEM (a and b) and TEM (c and d) images of manganese oxide and the GMP10 composite material; and (e) HR-TEM images of the GMP10 composite material.

*Mn<sub>x</sub>O<sub>y</sub>*, respectively (Fig. 4(e)). Therefore, the observed interplanar spacings for the GMP10 sample further confirm the polycrystalline nature of the material.

Fig. 5(a and b) shows the diffuse reflectance absorption spectra (DRS) for graphene, *Mn<sub>x</sub>O<sub>y</sub>*, and the composite samples at various pH values. Both the *Mn<sub>x</sub>O<sub>y</sub>* and composite samples exhibited strong UV absorption, but the *Mn<sub>x</sub>O<sub>y</sub>* sample showed the least visible-light absorption. In contrast, the composite samples displayed enhanced visible-light absorption, increasing from GMP12 to GMP8 due to the increasing *MnO<sub>2</sub>* content and the presence of graphene, which broadened the absorption band (Fig. 5(a)). Using the Kubelka–Munk model and the Tauc equation, the bandgaps for *Mn<sub>x</sub>O<sub>y</sub>*, GMP12, GMP10, and GMP8 were determined to be 1.72, 1.56, 1.42, and 1.3 eV, respectively. These results suggest that graphene and the *MnO<sub>2</sub>* components reduced the bandgap, thereby enhancing the electron–hole separation under visible light.

The BET-specific surface of all the samples was measured, and the results are presented in Fig. 5(c). The isotherms of all samples exhibit a hysteresis loop and are classified as type IV isotherms, indicating a porous material. Specifically, the BET-specific surface areas of GMP8, GMP10, GMP12 and *Mn<sub>x</sub>O<sub>y</sub>* were found to be 16.26, 25.16, 20.98 and 14.87 m<sup>2</sup> g<sup>-1</sup>, respectively. The enhanced surface area of the composite materials compared to that of bare *Mn<sub>x</sub>O<sub>y</sub>* is due to the uniform distribution of *Mn<sub>x</sub>O<sub>y</sub>* nanoparticles on the graphene supports, providing more active sites for photocatalytic activity.

The electrochemical impedance spectroscopy (EIS) results (Fig. 5(d)) show that the composite samples had a smaller Nyquist radius than the *Mn<sub>x</sub>O<sub>y</sub>* sample, indicating enhanced charge transfer, likely due to the highly conductive graphene component. Photocurrent measurements for the *Mn<sub>x</sub>O<sub>y</sub>*, GMP8–GMP12 samples were also performed (SI, Fig. S1). In 0.1 M Na<sub>2</sub>SO<sub>4</sub> solution, the GMP8–GMP12 heterojunction samples showed substantially higher photocurrents than the fabricated *Mn<sub>x</sub>O<sub>y</sub>* sample. The GMP10 sample produced the largest photocurrent, approximately three times that of *Mn<sub>x</sub>O<sub>y</sub>*. The photocurrent remained stable over many on/off light cycles,

indicating efficient charge separation and suppressed recombination. Together with the EIS data, these observations demonstrate improved charge separation and lower charge-transfer impedance than in the composite samples. Overall, the formation of heterojunctions in the composites reduces electron–hole recombination and enhances carrier separation, which explains the improved photocatalytic performance.

The photocatalytic activity of the manganese oxide/graphene composites was evaluated by monitoring the decolorization of MB dye in water using a 400 W Xenon lamp. As shown in Fig. 6(a and b), the removal efficiency of MB by the GMP8–GMP12 composite samples (with 20 mg of catalyst) was superior to that of the *Mn<sub>x</sub>O<sub>y</sub>* sample. In particular, the GMP10 sample exhibited the highest decomposition efficiency for MB, reaching 65.4% after 150 minutes of illumination (not including dark absorption). The GMP8 and GMP12 samples achieved degradation efficiencies of 40.8% and 53.1%, respectively, while the *Mn<sub>x</sub>O<sub>y</sub>* sample reached only 30.1%. These results indicate that the incorporation of graphene enhanced the photocatalytic performance of the composite samples, in which graphene not only served as a substrate for the *Mn<sub>x</sub>O<sub>y</sub>* nanoparticles, but also facilitated charge transfer. Using the Langmuir–Hinshelwood model ( $\ln(C_t/C_0) = -kt$ ), the reaction rate constants ( $k$ ) for the GMP12, GMP10, and GMP8 samples were determined to be 0.00495 min<sup>-1</sup>, 0.00716 min<sup>-1</sup>, and 0.00367 min<sup>-1</sup>, respectively. Table S1 compares the photocatalytic performance of the GMP10 composite sample with that reported in recent studies.

Experiments varying the amount of photocatalyst were performed to determine the optimal catalyst loading; the results are shown in Fig. 6(c). The results suggest that the photocatalytic degradation efficiency increased with catalyst loading from 20 mg to 120 mg, reaching a maximum degradation efficiency of 83.3%. However, when the catalyst amount was increased to 120 mg, the degradation efficiency decreased slightly to 81.2%. These results can be explained by the fact that the photocatalytic degradation efficiency increased as the amount of catalyst increased since there were more reaction sites. However, excessive catalyst concentrations can hinder light penetration and restrict the interaction between light and the catalyst's surface, reducing the photocatalytic efficiency.

Additionally, photocatalytic cycling experiments were performed to evaluate the reusability of the material. As shown in Fig. 6(d), the degradation efficiencies of MB with 80 mg of the GMP10 catalyst were 83.3%, 83.7%, 80.7%, and 78.4% in four consecutive cycles. These results indicate that the photocatalytic performance of GMP10 remained relatively stable over four cycles. Furthermore, we also performed post-characterizations of the photocatalyst after investigating its stability (Fig. 6e and f). The XRD patterns confirm that the crystallinity of the material was well preserved, while the post-stability SEM images show a negligible change.

The photocatalytic mechanism is illustrated in Fig. 7. The energy levels,  $E_C$  and  $E_V$ , are referenced from Zhao *et al.*<sup>24</sup> When *Mn<sub>x</sub>O<sub>y</sub>* is irradiated with light of energy greater than its bandgap, electron–hole pairs are generated on the surface of the *Mn<sub>x</sub>O<sub>y</sub>* particles. The photogenerated charges on the *Mn<sub>x</sub>O<sub>y</sub>* particles can participate in a series of redox reactions to form

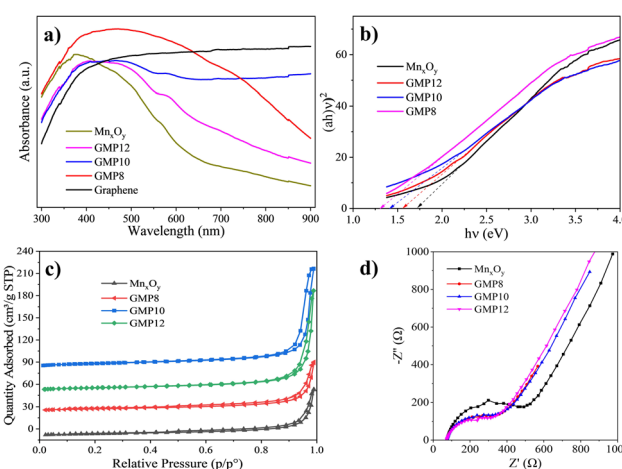


Fig. 5 (a) Diffuse reflectance absorption spectrum; (b) Tauc plots; (c) N<sub>2</sub> adsorption–desorption isotherms and (d) Nyquist plot of graphene, *Mn<sub>x</sub>O<sub>y</sub>*, and GMP8–GMP12 composite samples.



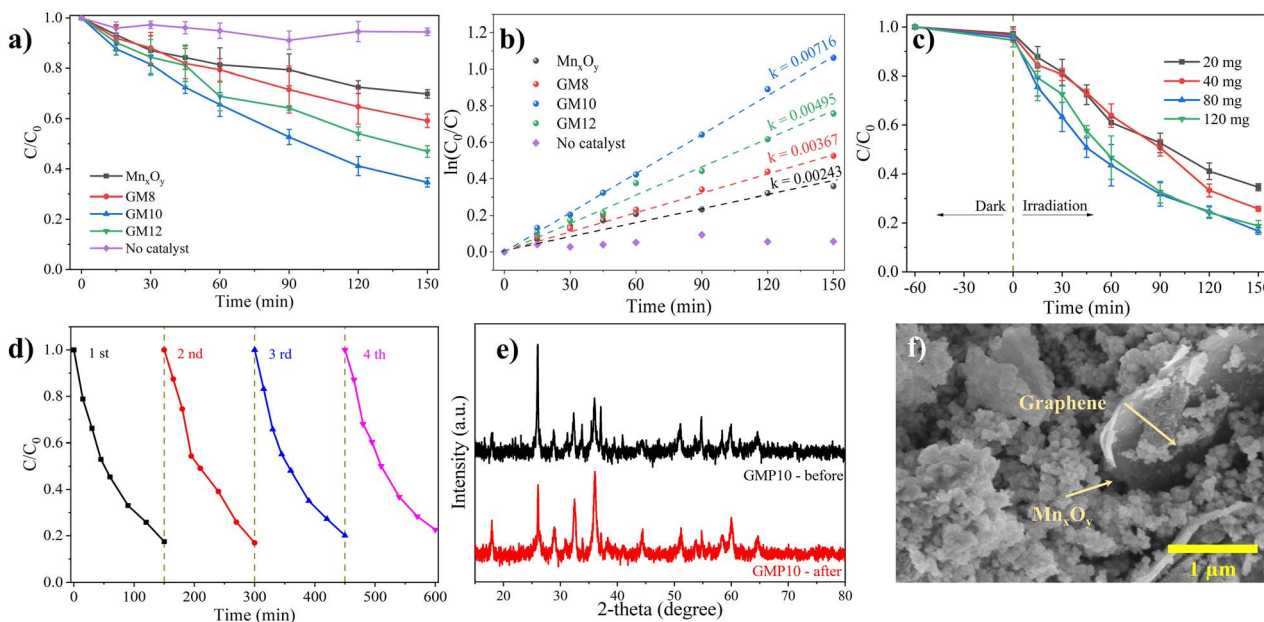


Fig. 6 Comparison of photocatalytic ability of  $\text{Mn}_x\text{O}_y$  and GMP8–GMP12 composite catalysts (catalyst dosage:  $m = 20 \text{ mg}$ ) for degrading MB dye: (a)  $C/C_0$  plot and (b)  $\ln(C_0/C)$  plot; (c) effects of the amount of GMP10 for MB decomposition; (d) photocatalytic cycling experiments of GMP10, using 80 mg of catalyst; (e) XRD patterns of GMP10 before and after stability test and (f) SEM of GMP10 after stability test.

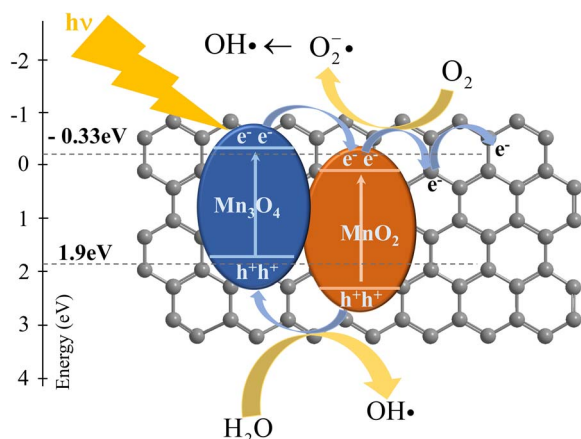
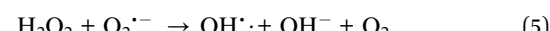
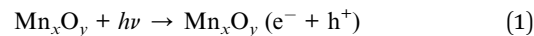


Fig. 7 Mechanism of MB photocatalysis by GMP10.

radicals on the catalyst's surface. These radicals can subsequently interact with the MB dye molecules adsorbed on the catalyst's surface, resulting in the formation of degradation products. During this process, the photogenerated charged particles on the  $\text{Mn}_x\text{O}_y$  particles can move to another location through the graphene, or to another particle (another oxide) due to the heterostructure, thus preventing recombination, which increases the photocatalytic degradation efficiency. Additionally, heterojunctions formed between the different  $\text{Mn}_x\text{O}_y$  phases (such as  $\text{Mn}_3\text{O}_4$ ,  $\text{MnO}_2$ , and  $\text{HMnO}_2$ ) may also contribute to the improved photocatalytic activity, as the photogenerated charge carriers can be rapidly transferred between these phases. Some of the representative reactions involved in the photocatalytic degradation process of  $\text{Mn}_x\text{O}_y$ -based materials are presented as follows:



The quenching experiments were also performed with the free radical scavengers: EDTA (photohole quencher,  $\text{h}^+$ ),

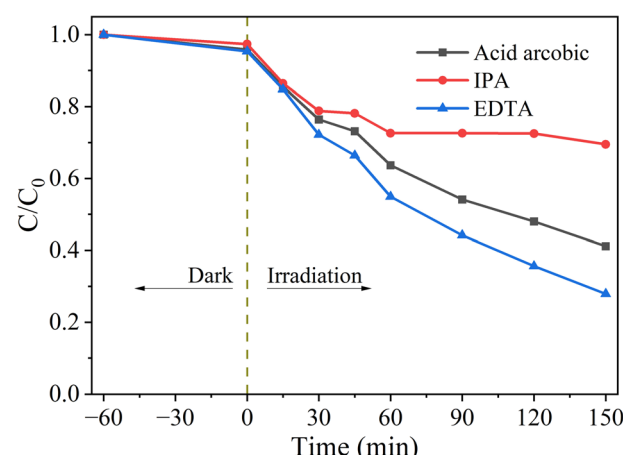


Fig. 8 Quenching experiments with EDTA, IPA, and AA quenchers.



isopropyl alcohol (IPA) (hydroxyl radical scavenger,  $\cdot\text{OH}$ ) and ascorbic acid (AA) (superoxide radical scavenger,  $\cdot\text{O}_2^-$ ). For each photocatalytic experiment, 8 mL of the scavenger solution (0.1 M) was added to suppress the main active species. The photocatalytic efficiency with AA, IPA, and EDTA as quenchers was 58.8%, 30.5% and 72.1%, respectively. The degradation efficiency for IPA as a quencher decreased most significantly, indicating that  $\cdot\text{OH}$  played a dominant role in the degradation process. The contribution of  $\cdot\text{O}_2^-$  also played a significant role, as shown by the reduced efficiency of 58.8%. Additionally,  $\text{h}^+$  participated in the degradation process, but its contribution was not much (Fig. 8).

## 4 Conclusions

In this study, manganese oxide/graphene composites were successfully fabricated using plasma-assisted electrochemical exfoliation combined with co-precipitation. The graphene component enhanced conductivity, improving the decomposition efficiency for MB. Adjusting the pH of the precursor solution ( $\text{NaOH}$  10% +  $(\text{NH}_4)_2\text{SO}_4$  5%) influenced the manganese oxide composition ( $\text{MnO}_2$ ,  $\text{Mn}_3\text{O}_4$ ,  $\text{MnOOH}$ ), enabling control over the material structures for specific applications. Photocatalytic evaluation under visible light revealed varying efficiencies due to material absorption, the graphene component, and heterojunctions within the composites. These findings offer a simple approach for developing graphene-based composites with diverse manganese oxide forms for the degradation of organic pollutants and other applications.

## Author contributions

Pham Huong Quynh: processed data and prepared the manuscript. Nguyen Thi Thu Phuong, Ta Thi Huong, Tran Y Doan Trang, Pham Thi Mai Huong, Vu Thi Thuy conducted experiments and processed data. Dang Van Thanh, Pham Nguyet Anh, Nguyen Thanh Trung helped with material characterization and provided critical comments. Dang Van Thanh, Vu Thi Thuy, Nguyen Long Tuyen conceived, designed, and supervised the experiments. All authors read and approved the final manuscript.

## Conflicts of interest

The authors declare no conflict of interest.

## Data availability

The supporting data has been submitted along with the manuscript and will be available as SI when the article online. See DOI: <https://doi.org/10.1039/d5ra03186a>.

## Acknowledgements

Authors would like to express their sincere gratitude to Hanoi University of Industry for sponsoring the project with grant number HD 66-2024-RD/HD-DHCN.

## References

- D. Zhou, Q. Liu, Q. Cheng, Y. Zhao, Y. Cui, T. Wang and B. Han, *Chin. Sci. Bull.*, 2012, **57**, 3059–3064.
- S. Jadhav, R. S. Kalubarme, C. Terashima, B. B. Kale, V. Godbole, A. Fujishima and S. W. Gosavi, *Electrochim. Acta*, 2019, **299**, 34–44.
- A. Pramitha, S. S. Hegde, B. R. Bhat, C. Yadav, S. Chakraborty, A. Ravikumar, S. D. George, Y. N. Sudhakar and Y. Raviprakash, *Phys. Scr.*, 2024, **99**, 105922.
- S.-L. Chiam, S.-Y. Pung and F.-Y. Yeoh, *Environ. Sci. Pollut. Res.*, 2020, **27**, 5759–5778.
- A. A. Amer, S. M. Reda, M. A. Mousa and M. M. Mohamed, *RSC Adv.*, 2017, **7**, 826–839.
- Y. Kong, R. Jiao, S. Zeng, C. Cui, H. Li, S. Xu and L. Wang, *Nanomaterials*, 2020, **10**, 367.
- R. Rajendiran, A. Patchaiyappan, S. Harisingh, P. Balla, A. Paari, B. Ponnala, V. Perupogu, U. Lassi and P. K. Seelam, *J. Water Process Eng.*, 2022, **47**, 102704.
- Y. Gu, J. Wu, X. Wang, W. Liu and S. Yan, *ACS Omega*, 2020, **5**, 18975–18986.
- M. Azarang, A. Shuhaimi, R. Yousefi and M. Sookhakian, *J. Appl. Phys.*, 2014, **116**, 084307.
- Z. Alves, C. Nunes and P. Ferreira, *Nanomaterials*, 2021, **11**(8), 2149.
- B. Saravanakumar, R. Mohan and S.-J. Kim, *Mater. Res. Bull.*, 2013, **48**, 878–883.
- R. Singhmar, S. Sahoo, S. Choi, J. H. Choi, A. Sood and S. S. Han, *Eur. Polym. J.*, 2024, **220**, 113462.
- Y. Wu, H. Yu, H. Wang and F. Peng, *Chin. J. Catal.*, 2014, **35**, 952–959.
- A. Hussain, A. Zahid, S. Ali, N. Khalid, A. Ashraf, A. Latif, M. A. Farrukh and M. Jabeen, *J. Taiwan Inst. Chem. Eng.*, 2024, **163**, 105642.
- M. Jarvin, S. A. Kumar, G. Vinodhkumar, E. Manikandan and S. S. R. Inbanathan, *Mater. Lett.*, 2021, **305**, 130750.
- L. Kamarasu, S. Sree Nannapaneni, S. Arunachalam, P. Arumugam and N. Kumar Katari, *Inorg. Chem. Commun.*, 2022, **145**, 109949.
- H. Visser, C. E. Dubé, W. H. Armstrong, K. Sauer and V. K. Yachandra, *J. Am. Chem. Soc.*, 2002, **124**, 11008–11017.
- Y. Zheng, W. Pann, D. Zhengn and C. Sun, *J. Electrochem. Soc.*, 2016, **163**, D230–D238.
- J. Zhao, J. Nan, Z. Zhao, N. Li, J. Liu and F. Cui, *Appl. Catal., B*, 2017, **202**, 509–517.
- P. Wu, S. Dai, G. Chen, S. Zhao, Z. Xu, M. Fu, P. Chen, Q. Chen, X. Jin and Y. Qiu, *Appl. Catal., B*, 2020, **268**, 118418.
- R. Yang, T. Tao, Y. Dai, Z. Chen, X. Zhang and Q. Song, *Catal. Commun.*, 2015, **60**, 96–99.
- F. Zeng, Y. Pan, Y. Yang, Q. Li, G. Li, Z. Hou and G. Gu, *Electrochim. Acta*, 2016, **196**, 587–596.
- X. Chen, X. Wang and D. Fang, *Fullerenes, Nanotubes Carbon Nanostruct.*, 2020, **28**, 1048–1058.
- J. Zhao, Z. Zhao, N. Li, J. Nan, R. Yu and J. Du, *Chem. Eng. J.*, 2018, **353**, 805–813.

